npj | materials degradation

Article

Published in partnership with CSCP and USTB

https://doi.org/10.1038/s41529-025-00639-x

Impact of hydrous species in surface alteration layer on mechanical properties of oxide glasses

Hongtu He[1,5], Jianxu Gong[1,5], Jiaxin Yu[1], Junyi Ma[2], Rui Wang[2], Linfeng Ding[3], Yuanzheng Yue[4] ✉ & Qiuju Zheng[2] ✉

Hydrogen bonds of hydrous species in the surface alteration layer are critical factor influencing the mechanical properties of glass. In this study, we revealed the underlying mechanism of this influence using the International Simple Glass (ISG), a boroaluminosilicate glass. Upon exposure to static corrosion in aqueous solutions at 121 °C for 90 min, the ISG surface layer underwent nearly complete leaching of network-modifying ions, leading to structural alterations and increased water content within the layer. Importantly, we found that both the water content and the hydrogen bonding strength of hydrous species in the alteration layer affect the mechanical properties of ISG. Strong hydrogen bonds enhanced the nano adhesion force of the glass surface, while reducing the nano-hardness, elastic modulus, and Vickers hardness of ISG. These findings provide insights into the relationship between interfacial chemistry and mechanical performance, helping design robust and durable glasses tailored for specific applications.

Under static conditions without the presence of mechanical stress, water molecules can react with glass surface via hydration, hydrolysis, and/or ion-exchange[1]. Such chemical reactions can lead to a variation in glass surface structure, e.g., formation of an alteration layer (AL), thus affecting the surface topography[2], density[3], thermal[4], optical[5], and electric properties[6]. The surface structural variation results in a chemo-mechanical coupling effect under mechanical stress. For instance, upon the Vickers indentation, the Vickers hardness and crack initiation resistance of many oxide glass systems can be significantly reduced with the increase in surface water content[7–9]. The nanohardness and elastic modulus of glass surface after water treatment are found to decrease with the water content within glass surface layer[7,10]. Water molecules can also diffuse into glass surface during the mechanical tests or sample polishing in water-containing environments, causing a decrease in nanohardness and elastic modulus of the glass surface layer[11,12]. Moreover, the mechanical properties of the glass surface layer are found to be dependent on the environmental humidity[12,13]. These findings clearly show that water affects the glass surface properties before, during, and after being in contact with water molecules.

In addition to the water content in glass surface layer, the hydrogen (proton) bond strength of the water in glass surface layer can also be altered[14]. One of the most efficient methods to probe the hydrogen bonding interaction of hydrous species (Si-OH and H_2O) in the AL is the sum frequency generation (SFG) spectroscopy, because this method allows precisely determining the dependence of the OH stretch vibration peak on the hydrogen bonding interaction. Various surface chemical treatments on the float soda lime silicate glass, such as SO_2 dealkalization and hydrothermal treatment[15–17], could generate the subsurface hydrous species within the surface layer, which are associated with multiple SFG sharp peaks in the OH stretch region. Based on the relative peak position in the OH stretch region of SFG spectra and MD simulations, it was found that upon the corrosion of borosilicate glass, the strong hydrogen bonds of hydrous species are predominant in the AL and the exact interfacial hydrogen bonding interactions of hydrous species depended on the corrosion environments[9,18]. To the best of our knowledge, the nature of hydrogen bonds (HBs) of hydrous species in the AL and its impact on mechanical properties of glass surface remains unclear, even though some efforts have been made to reveal the hydrogen bonding interaction of hydrous species in the AL[9,15–18].

To address the question how the hydrogen bonding interaction of hydrous species in the AL affects the mechanical properties of glass, in the present work, we studied the corrosion behavior of the International Simple

[1]Key Laboratory of Testing Technology for Manufacturing Process in Ministry of Education, Southwest University of Science and Technology, Mianyang 621010, China. [2]School of Materials Science and Engineering, Qilu University of Technology, Jinan 250353, China. [3]State Key Laboratory for Modification of Chemical Fibers and Polymer Materials, Engineering Research Center of Advanced Glass Manufacturing Technology, Ministry of Education, Donghua University, Shanghai 201620, China. [4]Department of Chemistry and Bioscience, Aalborg University, DK-9220 Aalborg, Denmark. [5]These authors contributed equally: Hongtu He, Jianxu Gong. ✉e-mail: yy@bio.aau.dk; qlzhengqj@163.com

Glass (ISG) (belonging to boroaluminosilicate system), which has been utilized as a host matrix for immobilizing radioactive wastes stemming from nuclear industry[18]. To mimic various corrosion conditions, all ISG samples were placed into 50 mL deionized water (unbuffered) in a pressure steam sterilizer for 0 min to 90 min at 121 °C. The water content and the HBs of hydrous species in the AL was probed by both the Raman and SFG spectroscopies. Atomic force microscopy (AFM), Time-of-flight secondary-ion mass spectroscopy (TOF-SIMS), and inductively coupled plasma-atomic emission spectrometer (ICP-AES) were used to characterize the surface roughness, chemical structure of the corroded layer, and the ions leached into the solution, respectively. The nanoindentation, nano-scratch, and adhesion tests were performed to reveal the evolution of mechanical properties with the alteration of glass surface by water corrosion. Based on the experimental results, we discussed the underlying mechanism of the HBs of hydrous species in AL on nanomechanical properties of ISG.

Results and discussion

Chemical structure of corroded glass surface

As the ISG is treated under accelerated corrosion conditions (Fig. 1a), the modifying ions including sodium (Na) and Calcium (Ca), are leached out of glass surface and diffused into the solution, while the network forming ions such as boron (B) and silicon (Si) are dissolved into the solution (Fig. 1b). As shown in Fig. 1b, all the network formers and modifiers are detected in the solution and their concentrations are determined using ICP-AES. The concentrations of the detected cations in the solution, particularly Si^{4+}, increase with extending the corrosion time (Fig. 1b), confirming that the structural network in the glass surface layer is gradually dissolved under the given corrosion conditions. Based on the mass balance of Si species detected in solution compared to the initial Si fraction in glass, the equivalent thickness of the dissolved glass surface layer can be determined[19], as shown in Fig. 1c. It is found that the equivalent thickness of the dissolved layer increases from ~518 nm to ~2170 nm as the corrosion time increases from 10 min to 90 min. Moreover, the topography of the corroded glass surface is obtained through the RMS roughness by AFM (Fig. 1d, e). It is seen that the roughness of various corroded glass surface remains almost unchanged (~ 0.4 nm).

The concentration of the modifying ions at the near-surface region can be varied through the leaching/dissolution process. To determine the ion distribution after the corrosion, the ToF-SIMS 3D images of network modifying ions distribution in glass surface are made (Fig. 2a), where more concentrated data points mean that more ions are present in glass surface. It is clearly seen that the Na and B ions are significantly depleted as the corrosion time extends to 90 min, while substantial protons are detected in the near-surface region. To further compare the ion distribution along the depth direction, the normalized concentration profile of specified ion across the distance to surface is determined, as shown in Fig. 2b–e. Prior to static corrosion, a slight depletion of Na in a range of ~500 nm occurs in the pristine ISG surface due to the evaporation of Na during the sample preparation process[20,21]. As the corrosion time extends from 0 to 10 min and 30 min, the B ion is not leached from glass surface, whereas the Na and Ca ions are leached out, leaving a relatively lower concentration of Na and Ca in the AL. The decrease of Na ion concentration is more pronounced than that of Ca, owing to the higher mobility and smaller radius of Na ion in ISG[19]. These findings imply that the corrosion of the ISG surface proceeds via an incongruent dissolution mechanism, as further supported by the ICP-AES analysis (Fig. 1b).

As the corrosion time extends to 90 min, the Na and B ions concentration decrease to almost zero and a nearly depleted region with a thickness of ~220 nm occurs in the glass surface, being consistent with ToF-SIMS 3D images (Fig. 2a). The Ca ion is almost retained in the near-surface region, and this is due to both the depletion of Na and B and the lower mobility of Ca than Na. Similar depletion of Na and B, as well as the retention of Ca in corroded ISG surface have been reported[22,23]. As Na and B ions are nearly depleted in the near-surface region, the water molecules from the aqueous solution diffuse into glass surface, resulting in an increase in hydrous species concentration. This is evidenced by the significant increase in proton concentration in the depleted region of AL, as shown in Fig. 2a, e. The diffusion of water molecules into AL also implies that the hydration process of glass surface occurs, especially upon the 90 min corrosion.

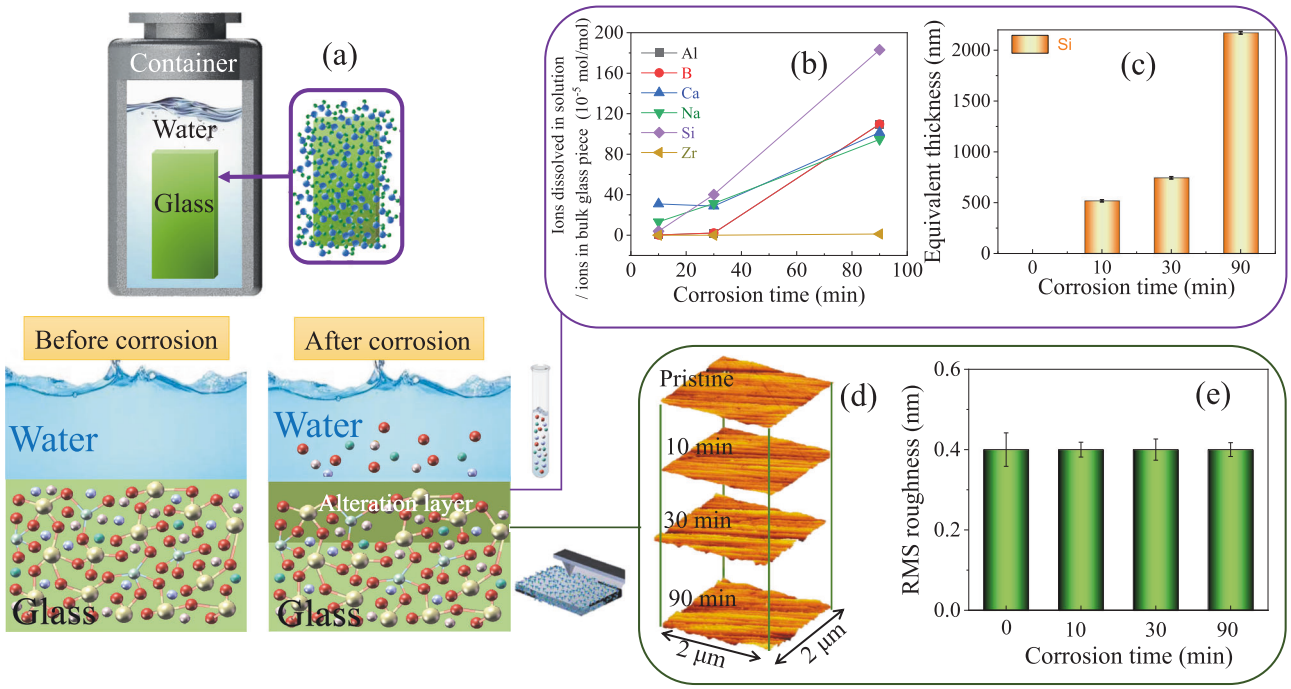

Fig. 1 | Glass corrosion behavior of ISG. a Schematic of the interaction between water and glass surface. **b** Molar concentration of the cations dissolved in deionized water, normalized by that of ions in bulk glass piece, as a function of corrosion time, as determined by ICP-AES analysis. **c** Equivalent thickness of altered glass calculated by silicon concentration under various corrosion conditions. **d** Topography of the corroded glass surface by AFM. **e** Root mean square (RMS) roughness of ISG surface as a function of corrosion time.

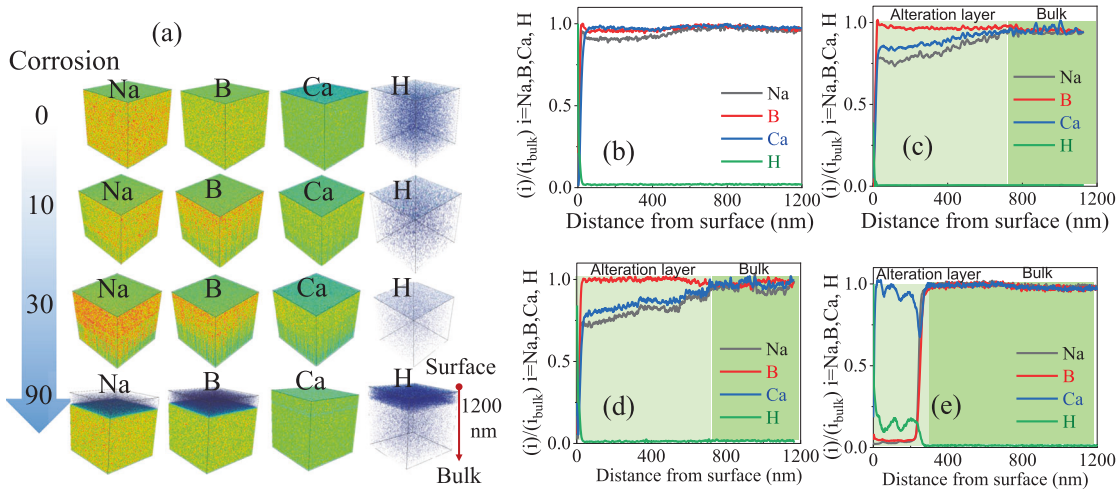

Fig. 2 | ToF-SIMS analyses of AL in corroded ISG surface. a ToF-SIMS 3D profile of ion distribution in ISG surfaces corroded for various corrosion time. The ion concentration as a function of distance from the surface when corroded for **b** 0 min, **c** 10 min, **d** 30 min, and **e** 90 min. The ion concentration is normalized to the silicon concentration at the same sputter depth and then normalized by the bulk concentration of each type of ion.

Hydrogen bonds of hydrous species in corroded glass surface layer

After the modifying ions are leached out from the glass surface, water molecules can either react the original non-bridging oxygen ions, forming hydroxyl groups (-OH), or diffuse into the AL as interstitial ones (H_2O). Figure 3a shows the Raman spectra of hydrous species in corroded glass surface under the room humidity condition (~ 40% RH). There is no detectable difference between the Si-O-Si linkages (~ 1050 cm^{-1}) and B-O-B linkages (~ 1400 cm^{-1}), whereas there is a significant increase in OH groups (~ 3100 cm^{-1}) in the subsurface region compared to the pristine glass, and the peak intensity for OH group increases with corrosion time (Fig. 3a). This suggests that the more hydrous species (Si-OH and H_2O) existed in the AL of ISG. Based on the Raman spectra, the total water content in the AL of the glass can be evaluated[24], as shown in Fig. 3c. It is seen that the total water content in the AL increases from ~0.1% to ~0.16% as the corrosion time extends from 0 min to 90 min (Fig. 3c). Note that the effective information depth of Raman spectra in the OH stretch region is ~1 μm, thus the result by Raman spectra indicates the total water content in glass surface layer. However, the spectral features of all hydrous species are masked since the maximum thickness of AL is <400 nm.

To reveal the HBs of hydrous species in the AL of corroded glass surface, SFG spectroscopy of various corroded glass surface is employed, as shown in Fig. 3b. Note that the SFG coherence length is less than 100 nm from the surface[25], thus useful information on hydrous species in the AL can be obtained, derived from the peak positions and relative intensities of the detected OH vibrations. All ISG surfaces show three peaks at ~3150, ~3350, and ~3790 cm^{-1}. The relatively weak peak at ~3790 cm^{-1} can be assigned to silanol groups on glass surface without hydrogen-bonding interactions with neighboring molecules[15,18,26]. The increase in the intensity of the peak at ~3790 cm^{-1} with the corrosion time implies an increase in the intensity of silanol groups or free OH on corroded ISG surface.

The peaks at <3650 cm^{-1} are the hydrous species groups with varying the strength of hydrogen bonding[15]. Since the desorption energies for HBs of hydrous species detected at <3600 cm^{-1} are higher than those of condensed water phases, the hydrous species are mostly water molecules at gradient-induced binding sites in the AL, not the physisorbed molecules on glass surface[16]. Generally, three types of HBs of the hydrous species (Si-OH and H_2O) can exist in the AL: (1) the HBs between water molecules; (2) the HBs between the oxygen of water and hydrogen of silanol (Si-OH); (3) the HBs between the bridging oxygen (BO) and the hydrogen of water. Based on the empirical and theoretical relationship between the OH stretch peak position and the O….H-O distance[18], the hydrogen bond lengths of the three types of HBs are determined to be approximately 0.18 nm, 0.172 nm, and 0.17 nm, respectively (Fig. 3e). The lower wavenumber component (~ 3150 cm^{-1}) in Fig. 3b is dominated by a very strongly HBs between the oxygen of water and hydrogen of silanol (Si-OH), while the higher wavenumber component (~ 3350 cm^{-1}) is dominated by a strongly HBs between water molecules. Moreover, the ratio of the peak area at ~3150 cm^{-1} increases with extending the corrosion time (Fig. 3d), indicating that the amount of very strongly HBs of hydrous species in the AL increases with the corrosion time. This means that as the corrosion time extends, the hydrogen-bonding of the hydrous species in AL is enhanced (Fig. 3e), i.e., the O-H…O distance is decreased[15,18,27]. The increased relative intensity of lower wavenumbers in OH vibrations by SFG measurements has been reported for corroded ISG surface at pH 9 for longer durations and pharmaceutical borosilicate glass surface at pH 7 for shorter durations[9,18], suggesting that the relative fraction of strong HBs of hydrous species in AL of these glasses also increases with corrosion time.

Mechanical properties of corroded glass surface

Since the hydrogen bonding strength of hydrous species in AL of glass is enhanced upon corrosion, the interfacial force to the corroded glass surface may be varied. Figure 4 shows the adhesion force between a diamond tip and various corroded ISG surfaces via AFM indentation. As the corrosion time extends from 0 to 90 min, the mean adhesion force increases from ~54 nN to ~95 nN (Fig. 4).

Generally, the adhesion force F_a at contact interface of sample/AFM tip is the sum of the capillary force (F_c), the van der Waals force (F_{vdw}), electric force (F_e), and chemical bonding force (F_b)[28]:

$$F_a = F_c + F_{vdw} + F_e + F_b \quad (1)$$

Note that all the ISG surface and diamond tip are kept in air for a sufficiently long time before adhesion measurements. The surface charge is expected to be fully dissipated, thus $F_e = 0$. F_b can also be neglected when the two surfaces are fully saturated with non-reactive functional groups. Therefore, F_a is dominated by F_c and F_{vdw}. In a humid environment, interfacial water molecules impinging from the gas phase may condense around the contact interface, thereby forming a meniscus bridge around the contact area[29]. Thus, both the F_c and F_{vdw} can be affected by the presence of water molecules within glass surface layer when tested in humid air, e.g., by the depth and HBs of water. Based on refs. 28,30, the depth of adsorbed water film can be estimated from both the relative humidity of 50% RH and

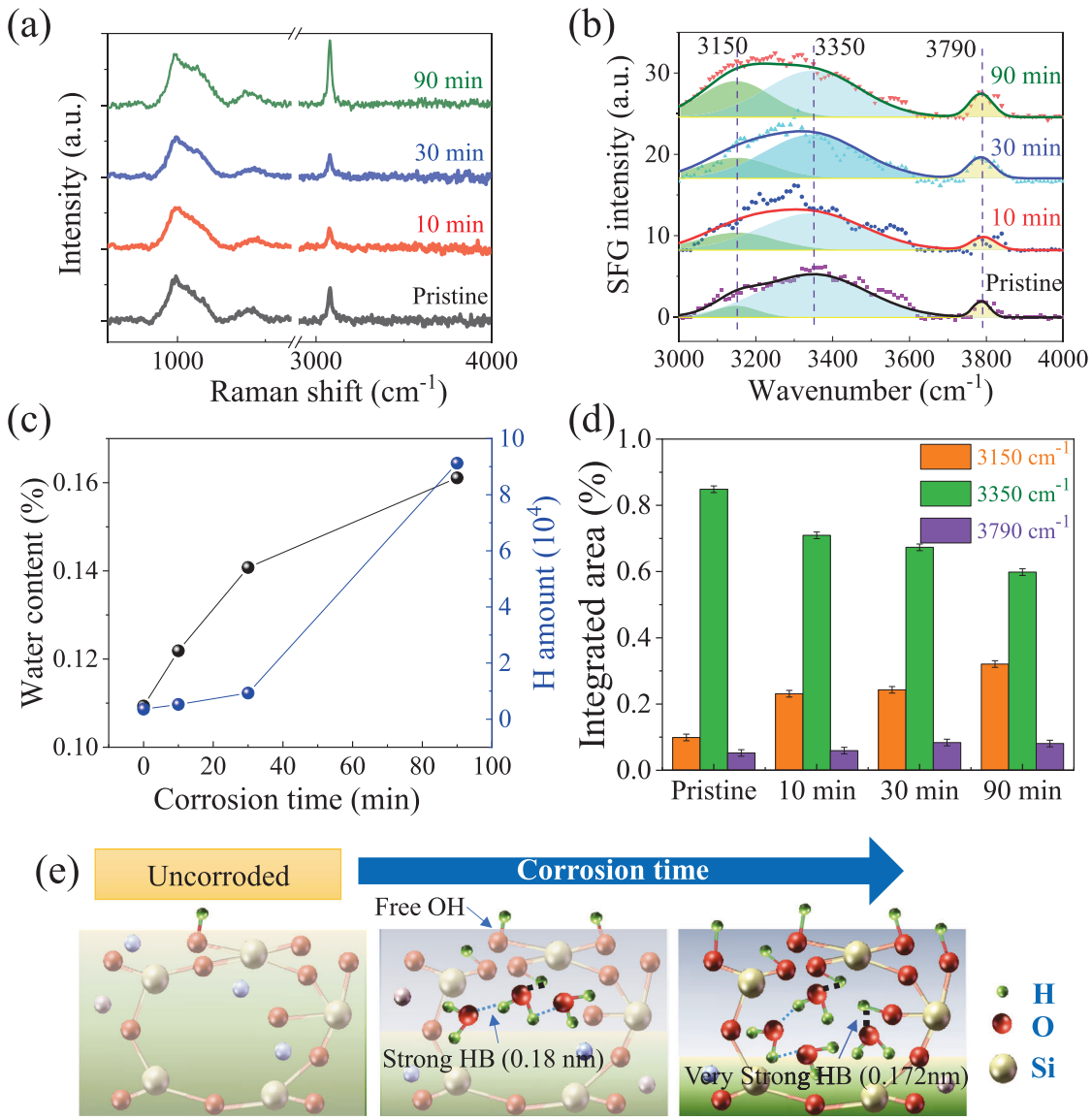

Fig. 3 | Hydrous species and HBs in corroded glass surface layer. a Raman spectra and **b** SFG spectra of various corroded glass surface. **c** Water content in the glass surface and hydrogen amount as a function of corrosion time. **d** Integrated area ratio between ~3150 cm^{-1} band (A_{3150}) and the ~3350 cm^{-1} band (A_{3350}) and ~3790 cm^{-1} band (A_{3790}) as a function of corrosion time. The error bar in **d** is determined based on the standard deviation of 4 measurements for each sample. **e** Schematic of the enhanced HBs of hydrous species in AL.

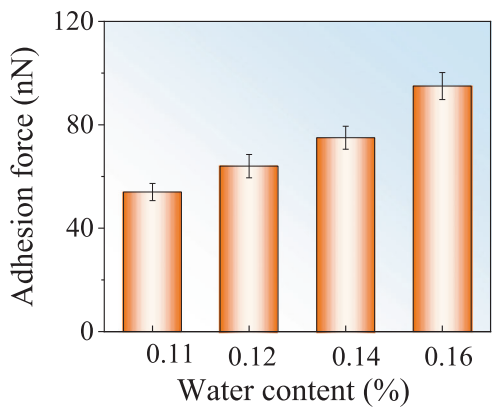

Fig. 4 | Adhesion force on corroded ISG surfaces. Adhesion force between the corroded ISG surface and diamond tip as a function of water content in the AL.

the water contact angles of diamond tip to ISG sample surfaces. However, the water contact angle on the corroded ISG surfaces does not vary with the corrosion time (Fig. S1 in Supporting Information), indicating that the depth of interfacial water film on corroded glass surface remains constant. The variation in the depth of adsorbed water film is not the key to the increase in interfacial adhesion force (Fig. 4b).

The next question is whether the HBs of hydrous species in the AL is responsible for the increased interfacial adhesion force of corroded ISG surface (Fig. 4b). Note that the surface energy of pure liquid water at room temperature is 72.8 ergs/cm^2, while that of strongly HBs of water (such as solid-like water) is close to the cohesion energy of ice (103.3 ergs/cm^2) due to the involvement of more hydrogen bonds per molecule[14,31]. Thus, we can infer that the presence of strong HBs of hydrous species in the AL can enhance the adhesion force. This is supported by the fact that F_a is enhanced by the growth of solid-like water on silicon surface, while it is significantly suppressed when the formation of solid-like water is prevented by the adsorption of gas-phase alcohol molecules[14]. Therefore, combining the SFG

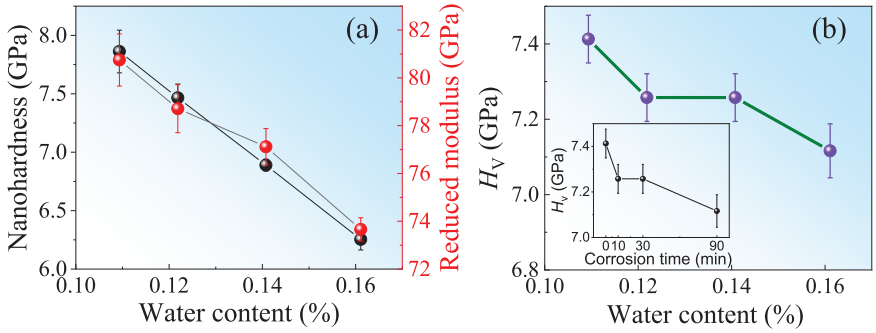

Fig. 5 | Nano- and Vickers indentation on corroded glass surface. a Nanohardness and reduced modulus and **b** Vickers hardness (H_v) of corroded ISG surface as a function of water content in the AL. Inset: the Vickers hardness as a function of corrosion time.

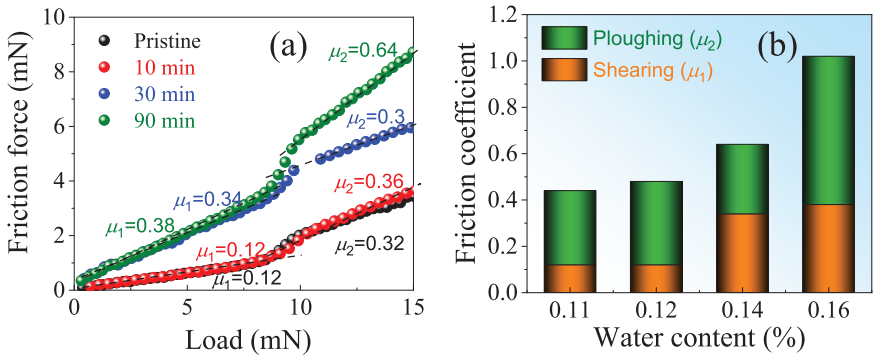

Fig. 6 | Nanoscratch analyses of various corroded glass surfaces. a Friction force on various corroded glass surfaces as a function of normal load during nanoscratch process. **b** Friction coefficient of shearing (μ_1) and ploughing (μ_2) on various corroded glass surfaces.

data (Fig. 3) and ref. 14, it is inferred that the increased strong HBs of hydrous species in the AL on corroded glass surface are responsible for the increase of the interfacial adhesion force. A similar increase in interfacial adhesion strength has been reported for hydrated glass surface layer[32].

Nanoindentation tests are carried out to measure the change of nanomechanical properties of ISG surface with varying corrosion conditions. The dependence of both nanohardness and reduced modulus of corroded ISG surfaces on the penetration depth is reflected in Fig. S2 in Supporting Information. Note that instead of elastic modulus, the reduced modulus is determined here due to the unknown Poisson's ratio of AL on corroded ISG surface. Evidently, as the corrosion time extends from 0 to 90 min, the reduced modulus of ISG surface decreases from ~80.7 to ~70.6 GPa, while the nanohardness of ISG surface decreases from ~7.8 to ~6.2 GPa (Fig. 5a). As shown in Fig. 5b, the Vickers hardness of ISG decreases from ~7.4 to ~7.1 GPa, as the corrosion time extends from 0 to 90 min (Fig. 5b), consistent with the changes of both nanohardness and reduced modulus (Fig. 5a). It is seen that the surface layers with modified chemical structures affect the mechanical properties of ISG at both nanoscale and macroscale. Once the mechanical properties of ISG at macroscale degrade, the probability of glass fracture upon physical contact increases, leading to a larger glass surface area and accelerated chemical corrosion in geological disposal environments. In other words, the force required to initiated cracking decreases in glasses with degraded mechanical properties. Consequently, crack propagation becomes more likely. When the crack reaches a critical size, the glass products may fail to meet functional requirement, and can no long be utilized. In such case, a portion of the immobilized radiative elements may become exposed to the environment. Therefore, the mechanical properties of glass products are critically linked to their service lifetime[33,34].

Both the modified structure and the presence of hydrous species within glass surface layer affect the mechanical properties of glass. Upon the attack of aqueous solution, the network structure within the glass surface layer becomes "silica-like" due to the leaching of modifying ions from the surface layer (Figs. 1, 2). If the "silica-like" structure is enriched in the surface layer of the corroded glass, both the nanohardness and Vickers hardness should be higher than those of the uncorroded surface considering the fully polymerized network of silica. However, the opposite trend is observed (Fig. 5), indicating that the hydrous species are the dominant structural factor within the glass surface layer. In fact, as the corrosion time extends, the water content in ISG surface increases (Fig. 3b), making glass surface more susceptible to the hydrolysis of the network structure of glass under stress condition[35]. Moreover, the structural network becomes more "strained" with a higher averaged Si-O-Si bond angle and shorter averaged Si-O bond length after corrosion[36]. Additionally, the hydrogen bond strength of hydrous species in the AL of corroded glass surface increases with extending corrosion time (Fig. 3b, d). These variations facilitate the transition state of the hydrolysis of Si-O-Si network with water molecules under stress condition during nanoindentation and Vickers indentation[9,35]. As a result, the indented depth and volume increase, leading to a reduction in both nanohardness and Vickers hardness (Fig. 5a, b). This can also explain both the decrease in nanohardness of glass surface layer with hydrated "silica-like" structure and the increase in nanohardness of glass surface layer with non-hydrated "silica-like" structure[2,10–12].

Both indentation tests performed in the surface normal direction and scratch tests conducted in the tangential direction provide critical insights into the actual physical contact behavior of ISG surface during practical applications. To understand the nanoscratch behavior of ISG surface after various corrosion process, the friction force on corroded ISG surface during the ramp loading process was plotted as a function of normal load, as shown in Fig. 6a. Both the scratch depth and residual depth of all corroded glass surfaces during the nanoscratching process increase with raising the normal load (Fig. S3 in Supporting Information). The friction force also increases with increasing the normal force (Fig. 6a), indicating the load-dependent friction mechanism in different loading regions. Thus, at the nanoscale, Amonton's law fails to explain the observed friction behavior, as the non-negligible adhesion force between the contacting surfaces significantly influences the frictional interactions (Fig. 4)[37]. This implies that, in addition to conventional frictional parameters, factors such as surface energy and adhesive interactions of AL, should be considered to accurately describe frictional mechanisms at such small scales. To reveal the friction

mechanism, the friction coefficient is evaluated based on the slope of the linear relation between the friction force and the normal force, as shown in Fig. 6a. It is seen that there are two friction coefficients that represent two stages of the friction process. The friction coefficient (μ_1) in the first stage is relatively lower than that in the second stage (μ_2) (Fig. 6a). According to Bowden and Tabor[38,39], the friction force is the sum of the shearing force related to adhesion and the ploughing force related to ploughing induced plastic deformation. Thus, it is reasonable to infer that the μ_1 in the first stage is affected by the adhesion force since the ploughing effect remains relatively low (Fig. S3 in Supporting Information). In contrast, the μ_2 of the second stage is significantly affected by the ploughing effect, arising from the relatively large plastic deformation of glass surface layer (Fig. S3 in Supporting Information).

During the first stage of nanoscratching, the μ_1 increases from ~0.12 to ~0.38 as the corrosion time extends from 0 to 90 min (Fig. 6b), this trend is associated with the increase of adhesion force with corrosion time (Fig. 4) since the shearing of interfacial adhesion junction plays a critical role[38]. The μ_2 increases from ~0.32 to ~0.64 as the corrosion time extends from 0 to 90 min (Fig. 6b). This can be explained by the significant increase in scratch depth observed during the nanoscratching process, especially after 90 min of corrosion, indicating a reduction in surface hardness and mechanical integrity. This increase in scratch depth is associated with the significantly increased depth of depletion layer up to ~250 nm (Fig. 2).

Substantial hydrous species (Si-OH and H_2O) exist in glass surface (Figs. 3, 4), and the depletion layer is softer than the bulk (Fig. 5), making the indenter tip penetrate the glass surface much easier owing to the stress corrosion effect[35]. However, after a certain duration of corrosion (e.g., 30 min and 90 min), the residual depth of corroded surface decreases. There are two possible reasons for the decrease in residual depth. First, the plasticity of the corroded glass surface with both substantial amounts of hydrous species (Si-OH and H_2O) and "silica-rich" structure gets lower[9], and consequently the residual depth of corroded glass surface decreases upon nanoscratching. Second, since the nanoscratching speed is relatively high (5 μm/s), the contact time of the tip to the surface during the nanoscratching becomes shorter (≤ 5 s), and hence, the water-induced hydrolysis is limited under stress conditions[35].

Water-glass interactions and its impact on the property degradation of glasses have been extensively studied[9,19]. Upon the static corrosion with aqueous solution, the water molecules can diffuse into the glass surface, and thus mobile ions in the structural network can be leached out, leading to a near-surface "silica-like" network structure. Water exists in glass either as a hydroxyl group (SiOH) when the total water content is ≤1000–3000 ppm or as interstitial molecular water when the total water content is even higher[40,41]. The total water content in glass surface has been found to play an important role in the variation of glass properties[2,3,6,7,9–11,42]. Nevertheless, less attention has been paid to the impact of the existing form of water on glass properties. The present study may give new insight into the relationship between the water-glass interaction and mechanical properties of glass surface. If the hydrogen bonding interaction of hydrous species in the AL of glass is stronger, the mechanical properties of glass surface, including nanohardness, reduced modulus, nanoscratch, and Vickers hardness, could become degraded, owing to the enhanced hydrolysis of network structure under stress conditions. This implies that not only the water content, but also the form of water in glass surface exerts strong influence on glass mechanical properties.

The above-mentioned changes of the mechanical properties can be explained in terms of the topological constraint theory. This is because the hydrous species in the AL constitute a sub-network that impacts the primary network structure, and hence the glass mechanical properties[43]. From the extended topological constraint concepts described elsewhere[44,45], it is known that the number and strength of modifying ion sub-network constraints can considerably affect glass properties, although its influence is smaller compared to that of the primary network constraints consisting of network-forming ions[44]. As described above, upon corrosion, the hydrous species replace the leached modifying ions (Na^+, Ca^{2+}), constituting a sub-network since they play a role as network modifiers. The subnetwork of hydrous species interpenetrates and depolymerizes the primary network structure involving Si, B, and Al. The hydrogen bonds in hydrous species within the AL break down the primary network constraints more drastically compared to the bonds between oxygen and alkali/alkaline earth ions for comparable molar fraction. This is why the T_g of vitreous silica significantly drops upon adding only a tiny amount (1–100 ppm) of hydroxyl groups[42]. This suggests that the hydrogen bond interaction makes the AL structure more depolymerized and softer, thereby lowering its hardness and elastic modulus compared with alkali and alkaline earth ions. In other words, an increase in the content of water species in AL makes the AL more vulnerable upon the external load or friction. As aforementioned, water species involves both strong and weak hydrogen bonds[46,47]. Compared to the weak hydrogen bonds, it is expected that the strong ones have higher capability to weaken Si-O, B-O, and Al-O bonds, thereby lowering the strength of the constraints in the primary structural network. As a consequence, nanohardness and elastic modulus of the AL of ISG is lowered (Fig. 5). This interpretation is based on the fact that glass properties depend not only on the numbers of the constraints of network structures, but also on the strength of the constraints[45]. However, a quantitative interpretation needs to be made by establishing a topological constraint model through characterizing the local structure of the AL of ISG. It should also be mentioned that several challenging questions remain unsolved. What distinguishes the hydrogen bonding interaction of absorbed versus adsorbed water within the glass surface layer? How can the variation of hydrogen bond strength of hydrous species in the AL of glass be quantitatively correlated with the mechanical strength of the glass surface? Answering these questions may require advanced computational modeling in the future.

In summary, the ToF-SIMS, SFG, and Raman spectroscopy data revealed the existence and the chemical structure of hydrous species within the international simple glass (ISG) surface layer after static corrosion. We found that as the corrosion time extended to 90 min, the modifying ions in the network at ISG surface were almost completely leached out, causing an increase in water content within glass surface layer. Not only the increased water content, but also the enhanced hydrogen bonding of hydrous species within the AL during aqueous corrosion altered the mechanical properties of ISG. Specifically, these two factors collectively contributed to an increase in adhesion and friction force at nanoscale, a reduction in both nanohardness and elastic modulus at nanoscale, and a decline in Vickers hardness. These findings offer new insights into the glass-water interaction and its influence on the mechanical properties of glass materials.

Methods

Sample preparation

The ISG samples with the chemical composition of $60.2SiO_2$-$3.8Al_2O_3$-$16B_2O_3$-$12.6Na_2O$-$5.7CaO$-$1.7ZrO_2$ (mol%) were prepared by conventional melt-quenching method[48]. The analytical reagent-grade chemicals: SiO_2, Al_2O_3, H_2BO_3, K_2CO_3, Na_2CO_3, $CaCO_3$, and ZrO_2 were used as raw materials. The raw materials were mixed in a ball mill for 5 h (h) and then melted in air in an alumina crucible at 1580 °C for 2 h. The melt was poured onto a brass plate in air and then the glass was annealed for 2 h at its glass transition temperature. The glass samples were cut into a size of 10 mm × 10 mm × 5 mm, where the six faces of glass sample were coarse-polished using 600-, 1500-, 3000-, and 6000-grit SiC papers and fine-polished with 1 μm and 80 nm diamond suspensions. Prior to static corrosion tests, the samples were cleaned first with distilled water and then with acetone under ultrasonication, and subsequently dried in an oven for 2 h. For the static corrosion tests, the ISG samples were placed into 50 mL deionized water (unbuffered) in a pressure steam sterilizer, as shown in Fig. 1a. The corrosion temperature was set to be 121 °C, while the corrosion durations were set to be 10, 30, and 90 min, respectively. The specific static corrosion condition was selected based on the MCC-5 Soxhlet method from the standard testing protocol for glass dissolution and leaching tests[49]. The concentrations of various ions in the solution after corrosion were determined using ICP-AES (Thermo Fisher iCAP7400).

ToF-SIMS analysis of corroded ISG surface

After the static corrosion tests, the depth profile of each element in the glass surface was determined by the Time-of-flight secondary-ion mass spectroscopy (TOF-SIMS 5-100, ION-TOF GmbH, Germany). The acceleration voltage of the Bi^+ primary ion beam was 30 keV. The scanning area was $50 \times 50\ \mu m^2$ for the negative secondary ion detection with an incidence angle of 45° to the surface normal direction. The acceleration voltage of the O^{2+} Sputter ion beam was 1 keV, and the scanning area was $200 \times 200\ \mu m^2$ for negative secondary ion detection with an incidence angle of 45° to the surface normal direction.

Raman spectroscopy analysis of corroded ISG surface

The microstructure of the corroded glass surface was analyzed using a confocal micro-Raman spectroscope (Renishaw In Via, Renishaw, UK) in the range from 400 to 4000 cm^{-1} with a resolution of 2 cm^{-1}.

SFG measurements

The SFG spectroscopy was used to detect the HBs of the hydrous species in corroded glass surface under the environment humidity of 40% RH and at the temperature of 20 ± 0.5 °C. During the SFG measurements, visible light ω_{VIS} and infrared light ω_{IR} were adjusted to overlap in space and time, resulting in a sum signal ω_{SFG}, where the signal strength can be expressed as $\omega_{SFG} = \omega_{VIS} + \omega_{IR}$. In the present study, both visible pulses (532 nm) and tunable IR pulses (2.5–10 μm) generated with the EKSPLA laser system were spatially and temporally overlapped at the ISG surface. The incident angles of visible and IR pulses were 50° and 55° with respect to the surface normal direction, respectively. The SFG signal intensity was normalized by the intensities of input visible and IR beams, while the polarization combination for the collected spectra was *s* for SFG signal, *s* for visible beam, and *p* for IR beam (*ssp*).

Nanoindentation and nanoscratch analyses

Nanoindentation tests were conducted with a Berkovich diamond tip upon a nanomechanical tester (Agilent G200, Keysight, USA). The indentation depth was set to be 300 nm. Vickers indentation tests of glass substrates were performed by Vickers hardness tester (HXD-1000TMC/LCD, Shanghai Taiming Optics Co. Ltd, China). The normal load was set as 3 N. At least fifteen indents were made on each glass specimen to obtain accurate statistical values, and the measurements were performed in humid air (50% RH) at 23 ± 0.5 °C. Nanoscratch tests were conducted with a conospherical tip by a nanomechanical tester (Agilent G200, Keysight, USA). The nominal radius of the conospherical tip was 2 μm. The applied normal load was 15 mN with a ramp loading mode, the scratch distance was 50 μm, and the scratch speed was 5 μm/s. Each nanoscratch experiment procedure was composed of three steps. First, a pre-scan with a constant normal load of 10 μN was performed to obtain the initial glass surface topography. Second, the tip moved back to the initial position and began to scratch the glass surface under a given scratch load and speed, then the friction force and penetration (scratch) depth during nanoscratching were recorded simultaneously. Third, a post-scan was carried out with the same tip at a normal load of 10 μN to get the residual depth profile of the nanoscratch along the scratch direction. To avoid possible artifacts of the deformed zone induced by adjacent nanoscratches, every scratch test was conducted with at least ~30 μm separation distance. Total four scratch tests were performed under each testing condition to ensure the repeatability of the experiments, and only representative data are shown in this paper.

Nano-adhesion measurements

All adhesion tests were carried out by an AFM system (SPI3800N, Seiko, Japan), where the force-displacement curves were obtained from the pull-off measurement and a cubic corner diamond tip with a nominal radius of ~540 nm (Micro Star Technologies, USA). The spring constants of the tip cantilevers were ~254 N/m. During the AFM adhesion tests, the diamond AFM tip approached the surface and penetrates up to 50 nm before retracting, and the force-displacement curves of the diamond tip were recorded synchronously, providing insights into the adhesion and mechanical response of the glass surface. The separation points and adhesion force between the tip and glass surface were determined from force-displacement curves (Fig. S4 in Supporting Information). The mean adhesion force was determined through statistically analysis of 20 data points.

Data availability

The data supporting the main findings are available within the manuscript and supplementary information. Additional supporting data can be obtained from the corresponding authors upon reasonable request.

Received: 9 May 2025; Accepted: 3 July 2025;
Published online: 18 July 2025

References

1. Cailleteau, C. et al. Insight into silicate-glass corrosion mechanisms. *Nat. Mater.* **7**, 978–983 (2008).
2. Tadjiev, D. R. & Hand, R. J. Surface hydration and nanoindentation of silicate glasses. *J. Non-Cryst. Solids* **356**, 102–108 (2010).
3. Mei, H. et al. Effects of water on the mechanical properties of silica glass using molecular dynamics. *Acta Mater.* **178**, 36–44 (2019).
4. Sørensen, S. S. et al. Water as a modifier in a hybrid coordination network glass. *Small* **19**, 2205988 (2023).
5. Acocella, J., Tomozawa, M. & Watson, E. B. The nature of dissolved water in sodium silicate glasses and its effect on various properties. *J. Non-Cryst. Solids* **65**, 355–372 (1984).
6. Takata, M., Acocella, J., Tomozawa, M. & Watson, E. B. Effect of water content on the electrical conductivity of $Na_2O \cong 3SiO_2$ glass. *J. Am. Ceram. Soc.* **64**, 719–724 (1981).
7. Suratwala, T. I., Steele, R. A., Wilke, G. D., Campbell, J. H. & Takeuchi, K. Effects of OH content, water vapor pressure, and temperature on sub-critical crack growth in phosphate glass. *J. Non-Cryst. Solids* **263**, 213–227 (2000).
8. Sheth, N. et al. Effects of acid leaching treatment of soda-lime silicate glass on crack initiation and fracture. *J. Am. Ceram. Soc.* **104**, 4550–4558 (2021).
9. Zheng, Q. et al. Impact of the aqueous corrosion induced alteration layer on mechanical properties of pharmaceutical glasses. *npj Mater. Degrad.* **8**, 17 (2024).
10. Jiang, B., He, H., Zhang, Y. & Yu, J. Effects of water immersion and humid weathering on the near-surface mechanical properties of phosphate laser glass. *J. Am. Ceram. Soc.* **102**, 2462–2471 (2019).
11. Hackett, B. L., Wereszczak, A. A. & Pharr, G. M. Effect of aqueous-based mechanical polishing on the nanoindentation response of borosilicate glasses. *Int. J. Appl. Glass Sci.* **10**, 302–306 (2019).
12. Hirao, K. & Tomozawa, M. Microhardness of SiO_2 glass in various environments. *J. Am. Ceram. Soc.* **70**, 497–502 (1987).
13. He, H., Qiao, Q., Xiao, T., Yu, J. & Kim, S. H. Effect of humidity on friction, wear, and plastic deformation during nanoscratch of soda lime silica glass. *J. Am. Ceram. Soc.* **105**, 1367–1374 (2022).
14. Xiao, C. et al. Thickness and structure of adsorbed water layer and effects on adhesion and friction at nanoasperity contact. *Colloids Interfaces* **3**, 55 (2019).
15. Sheth, N., Luo, J., Banerjee, J., Pantano, C. G. & Kim, S. H. Characterization of surface structures of dealkalized soda lime silica glass using X-ray photoelectron, specular reflection infrared, attenuated total reflection infrared and sum frequency generation spectroscopies. *J. Non-Cryst. Solids* **474**, 24–31 (2017).
16. Luo, J., Banerjee, J., Pantano, C. G. & Kim, S. H. Vibrational sum frequency generation (SFG) spectroscopy study of hydrous species in soda lime silica (SLS) float glass. *Langmuir* **32**, 6035–6045 (2016).
17. Luo, J., Huynh, H., Pantano, C. G. & Kim, S. H. Hydrothermal reactions of soda lime silica glass-Revealing subsurface damage and alteration

of mechanical properties and chemical structure of glass surfaces. *J. Non-Cryst. Solids* **452**, 93–101 (2016).
18. Ngo, D. et al. Hydrogen bonding interactions of H_2O and SiOH on a boroaluminosilicate glass corroded in aqueous solution. *npj Mater. Degrad.* **4**, 1 (2020).
19. Gin, S. et al. Origin and consequences of silicate glass passivation by surface layers. *Nat. Commun.* **6**, 6360 (2015).
20. Sekine, T., Suzuki, T. & Yamamoto, K. Inward migration of glass-modifier cations during heat treatment under an N_2 atmosphere. *J. Am. Ceram. Soc.* **98**, 1464–1470 (2015).
21. Banerjee, J., Bojan, V., Pantano, C. G. & Kim, S. H. Effect of heat treatment on the surface chemical structure of glass: oxygen speciation from in situ XPS analysis. *J. Am. Ceram. Soc.* **101**, 644–656 (2018).
22. Collin, M. et al. Structure of International Simple Glass and properties of passivating layer formed in circumneutral pH conditions. *npj Mater. Degrad.* **2**, 4 (2018).
23. Collin, M., Fournier, M., Charpentier, T., Moskura, M. & Gin, S. Impact of alkali on the passivation of silicate glass. *npj Mater. Degrad.* **2**, 16 (2018).
24. Bonechi, B. et al. Micro-Raman water calibration in ultrapotassic silicate glasses: Application to phono-tephrites and K-foidites of Colli Albani Volcanic District (Central Italy). *Chem. Geol.* **597**, 120816 (2022).
25. Wei, X., Hong, S. C., Lvovsky, A. I., Held, H. & Shen, Y. R. Evaluation of surface vs bulk contributions in sum-frequency vibrational spectroscopy using reflection and transmission geometries. *J. Phys. Chem. B* **104**, 3349–3354 (2000).
26. Luo, J. et al. Thermal poling of soda-lime silica glass with nonblocking electrodes-Part 1: effects of sodium ion migration and water ingress on glass surface structure. *J. Am. Ceram. Soc.* **99**, 1221–1230 (2016).
27. Wang, H. et al. Vibrational density of states of strongly H-bonded interfacial water: insights from inelastic neutron scattering and theory. *J. Phys. Chem. C.* **118**, 10805–10813 (2014).
28. Xiao, X. & Qian, L. Investigation of humidity-dependent capillary force. *Langmuir* **16**, 8153–8158 (2000).
29. Barthel, A. J., Al-Azizi, A., Surdyka, N. D. & Kim, S. H. Effects of gas or vapor adsorption on adhesion, friction, and wear of solid interfaces. *Langmuir* **30**, 2977–2992 (2014).
30. Qian, L., Tian, F. & Xiao, X. Tribological properties of self-assembled monolayers and their substrates under various humid environments. *Tribol. Lett.* **15**, 169–176 (2003).
31. Douillard, J. & Henry, M. Calculation of surface enthalpy of solids from an ab initio electronegativity based model: case of ice. *J. Colloid Inter. Sci.* **263**, 554–561 (2003).
32. Michalske, T. A., Bunker, B. C. & Keefer, K. D. Mechanical properties and adhesion of hydrated glass surface layer. *J. Non-Cryst. Solids* **120**, 126–137 (1990).
33. Connelly, A. J., Hand, R. J., Bingham, P. A. & Hyatt, N. C. Mechanical properties of nuclear waste glasses. *J. Nucl. Mater.* **408**, 188–193 (2011).
34. Lu, X. et al. Effect of vanadium oxide addition on thermomechanical behaviors of borosilicate glasses: Toward development of high crack resistant glasses for nuclear waste disposal. *J. Non-Cryst. Solids* **515**, 88–97 (2019).
35. Ciccotti, M. Stress-corrosion mechanisms in silicate glasses. *J. Phys. D: Appl. Phys.* **42**, 214006 (2009).
36. Ogrinc, A. L., Zhou, Y., Hahn, S. H., Lin, Y. T. & Kim, S. H. Revealing the structure of the sodium-leached layer of soda lime silica glass: A comprehensive spectroscopic analysis. *J. Non-Cryst. Solids* **600**, 121989 (2023).
37. Persson, B. N. J. et al. On the origin of Amonton's friction law. *J. Phys. Conden. Matter* **20**, 395006 (2008).
38. Zhao, X., Peng, Y., Cao, X., Yu, C. & Lang, H. Robust superlubric interface across nano- and micro-scales enabled by fluoroalkylsilane self-assembled monolayers and atomically thin graphene. *ACS Appl. Mater. Inter.* **13**, 56704–56717 (2021).
39. Jia, Q. et al. Effects of structure relaxation and surface oxidation on nanoscopic wear behaviors of metallic glass. *Acta Mater.* **232**, 117934 (2022).
40. Amma, S., Kim, S. H. & Pantano, C. G. Analysis of water and hydroxyl species in soda lime glass surfaces using Attenuated Total Reflection (ATR)-IR spectroscopy. *J. Am. Ceram. Soc.* **99**, 128–134 (2016).
41. Stuke, A., Behrens, H., Schmidt, B. C. & Dupree, R. H_2O speciation in float glass and soda lime silica glass. *Chem. Geol.* **229**, 64–77 (2006).
42. Yue, Y. Anomalous enthalpy relaxation in vitreous silica. *Front. Mater.* **2**, 54 (2015).
43. Smedskjaer, M. M., Mauro, J. C. & Yue, Y. Prediction of glass hardness using temperature-dependent constraint theory. *Phys. Rev. Lett.* **105**, 115503 (2020).
44. Hermansen, C., Mauro, J. C. & Yue, Y. A model for phosphate glass topology considering the modifying ion sub-network. *J. Chem. Phys.* **140**, 154501 (2014).
45. Hermansen, C., Rodrigues, B. P., Wondraczek, L. & Yue, Y. An extended topological model for binary phosphate glasses. *J. Chem. Phys.* **141**, 244502 (2014).
46. Li, C. et al. In situ probing electrified interfacial water structures at atomically flat surfaces. *Nat. Mater.* **18**, 697–701 (2019).
47. Ma, X. et al. Hydrogen-bond network promotes water splitting on the TiO_2 Surface. *J. Am. Ceram. Soc.* **144**, 13565–13573 (2022).
48. Ryan, J. V. et al. ISG-2: Properties of the second International Simple Glass. *npj Mater. Degrad.* **7**, 47 (2023).
49. Thorpe, C. L. et al. Forty years of durability assessment of nuclear waste glass by standard methods. *npj Mater. Degrad.* **5**, 61 (2021).

Acknowledgements

H. H. and J. Y. acknowledge the funding from Sichuan Science and Technology program (Grant No. 2024NSFSC0147 and 2024NSFTD0019), Q. Z. acknowledge the funding from National Natural Science Foundation of China (Grant No. 52372006), Taishan Youth Scholar Project of Shandong Province (No. 202211209), and Shandong Major Science and Technology Innovation Project (2022CXGC010509). The funders played no role in study design, data collection, analysis, and interpretation of data, or the writing of this manuscript.

Author contributions

H.H., Y.Y. and Q.Z. conceived the project. Q.Z. processed the sample in the laboratory. R.W. processed and interpreted the ToF-SIMS and ICP data. J.M. performed the SFG experiments and interpreted the data. H.H. and J.G. performed the Vickers indentation, nanoindentation, and nanowear tests. Q.Z. and H.H. prepared the manuscript draft. J.Y., L.D., and Y.Y. participated in valuable discussions and provided useful feedback during manuscript preparation. All authors contributed to reviewing the final manuscript.

Competing interests

The authors declare no competing interests.

Additional information

Supplementary information The online version contains supplementary material available at https://doi.org/10.1038/s41529-025-00639-x.

Correspondence and requests for materials should be addressed to Yuanzheng Yue or Qiuju Zheng.